Structure-Composition Relationships for Mg-Ni and Mg-Fe Olivine

Arianna M. Morfin [a,b], C. Heath Stanfield [a,c]*, Madeline A. Murchland [a,d], Madeline F. Bartels [a,e], Alexandra B. Nagurney [a], Quin R.S. Miller [a]*, H. Todd Schaef [a]

[a] Energy and Environment Directorate, Pacific Northwest National Laboratory, Richland, Washington, 99354 USA
[b] Yakima Valley College, Yakima, Washington, 98902 USA
[c] Department of Geophysical Sciences, University of Chicago, Chicago, Illinois, 60637 USA
[d] Department of Earth and Spatial Sciences, University of Idaho, Moscow, Idaho, 83844 USA
[e] Department of Earth and Planetary Sciences, Yale University, New Haven, Connecticut, 06520 USA

KEYWORDS: Substitution; Nickel; Carbon Mineralization; Critical Minerals; X-ray diffraction

ABSTRACT: Olivine is a dynamic and important mineral in the crust and mantle with relevance to processes important to climate change technology, such as geologic carbon storage and critical mineral recovery. In this work, we critically evaluated and compiled a new database of olivine diffraction data, lattice parameters, and composition to enable rapid Ni-Mg-Fe olivine composition determination. A compilation of olivine X-ray diffraction data and chemical compositions from both the literature and the International Centre for Diffraction Data (ICDD) powder database was assembled to plot both the forsterite-fayalite and forsterite-liebenbergite solid solution lines. We present an expanded dataset to delineate equations and relationships used for quantifying the correlations between olivine lattice parameters and chemical compositions in Mg_2SiO_4-Fe_2SiO_4 (forsterite-fayalite) and Mg_2SiO_4-Ni_2SiO_4 (forsterite-liebenbergite) olivine solid solution series.

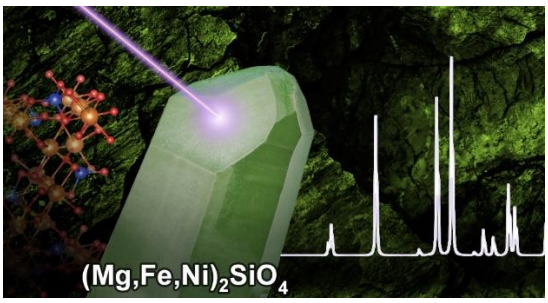

INTRODUCTION

Olivine is one of the most abundant and important minerals in the Earth due it's prevalence in the upper mantle and its involvement in natural geologic processes[2] including: the rheology of the mantle[3], formation of magmatic Ni-Cu sulfide deposits[4-9], and sources of mantle derived magma[10-12]. Understanding olivine and olivine-type structures and their properties is also important for the development of energy storage materials[13-19].

Olivine dissolution[20-23] and carbonation[24-83] reactions have been extensively explored as a potential pathway for anthropogenic CO_2 storage via mineralization and carbon dioxide removal (CDR) as the reaction of olivine and carbon dioxide produces stable carbonate minerals[36, 48-50, 54, 64, 84-95]. Olivine has been explored for CDR in multiple settings including: enhanced weathering[96], ex situ mineralization of mine tailings[97-99], and in situ mineralization of olivine-rich rocks[27, 47, 87, 88, 91, 100-120] (e.g. peridotites). Overall, accurate compositional characterization of olivine is key to evaluating a reservoir for carbon mineralization potential as this can inform calculations for overall carbon mineralization potential as well as recovery of critical minerals based on the divalent cations present in the olivine structure[121], since olivine carbonation reactions have also been shown to mobilize trace metals present within the olivine structure[122-130].

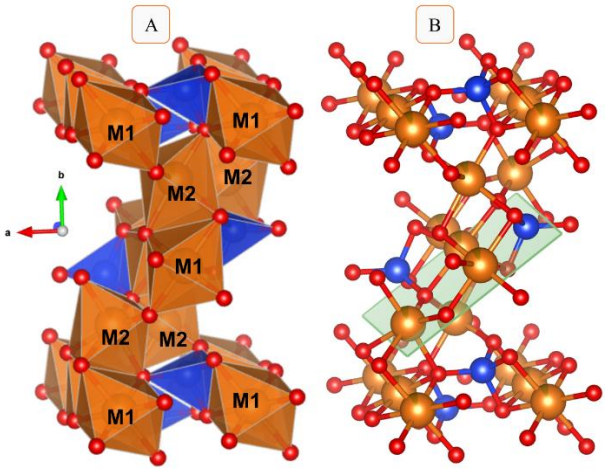

Figure 1. VESTA[1] crystal structure of forsteritic olivine using a polyhedral model (A) with M1 and M2 cation sites labeled and using a ball and stick model (B) with the d_{130} lattice plane highlighted in green. Orange, blue and red spheres represent Mg, Si, and O, respectively. The grey inclusion within the Mg spheres represents Fe.

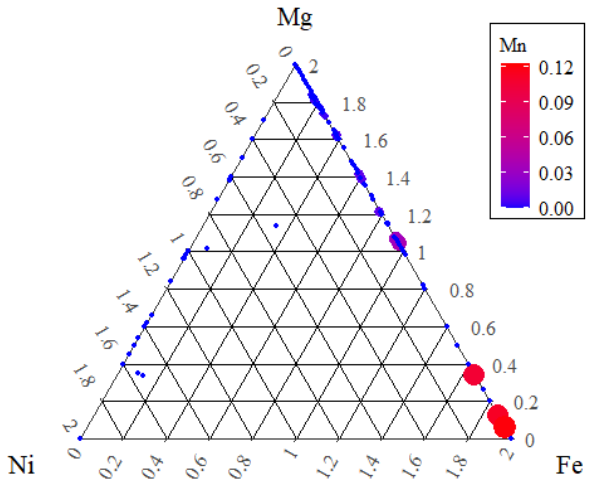

Figure 2. Ternary plot of all data points used in this study, including both Fo-Fa (Mg-Fe) and Fo-Lbb (Mg-Ni) solid solutions. Vertices represent endmember minerals. Points are scaled by Mn content (apfu) in both color and size.

Natural olivine may contain up to ~7000 ppm Ni[131] in its structure by substitution with divalent metal cations (e.g. Mg and Fe) and Ni tends to preferentially substitute into the M1 cation site[132-139], which is smaller and more distorted, compared to the M2 site (**Figure 1A**). Other divalent metals that can substitute into the olivine structure include Mn, Ca, Co, Be, and Zn, and these olivine structure minerals (Tephroite, Calcio-olivine, Co-olivine, Phenakite, and Willemite, respectively) are useful model minerals for unraveling mineral transformation reactions[70, 140]. Ni is of importance to this study as it has received the designation of a 'critical mineral' due to its depleted supply, high demand, and important role in many green technologies[141], such as energy storage systems (i.e. batteries), wind, solar, and nuclear energy[142-144]. Although Mn is also considered a critical mineral[141], olivine in mafic-ultramafic rocks targeted for carbon mineralization have higher abundances of Ni than Mn[145-147], and Mn-olivine (Tephroite) primarily occurs in metamorphosed skarn deposits and Zn ores[148]. In general, the composition of olivine is such that the greater the Mg content of the olivine crystal or region, the greater the Ni content[149], though there is some variation, primarily due to the presence or absence of sulfide minerals[131]. Therefore, determining the Mg content of an olivine sample can provide an indication of the Ni content of the olivine, and therefore guide the assessment of nickel recovery potential. Compositional characterization of olivine in a reservoir can be utilized to evaluate a site for carbon storage coupled with critical mineral recovery, which can lead to carbon negative mining and an additional source of revenue for carbon capture and storage projects.

X-ray diffraction (XRD), and specifically powder XRD, are important tools for identifying minerals and determining the lattice parameters of a sample. XRD analysis and refinements allow for relatively fast characterization of these important mineral properties. Previous studies have compiled data from scans of olivine along the solid solutions of forsterite (Fo)-fayalite (Fa) (Mg-Fe) and forsterite-liebenbergite (Lbb) (Mg-Ni). Schwab and Kustner 1977[150] compiled data for Fo-Fa olivine and constructed an equation to relate the composition of an olivine to its d_{130} spacing (**Figure 1B**). Morrison et al, 2018[151], performed a similar yet more extensive and statistically robust data compilation and constructed equations for determining Fe and Mg content based on the *b* lattice parameter of forsterite-fayalite. However, these two studies did not consider the effects of common cation substitutions[152, 153] in olivine when constructing their structure-composition relationships.

In our present study, we compiled literature data and International Center for Diffraction Data (ICDD) powder diffraction database files to further quantify the relationships of olivine lattice parameters and chemical compositions for Fo-Fa and Fo-Lbb olivine solid solutions with an expanded database. These relationships are presented in the forms of equations relating the unit cell parameters and d_{130} spacings of the olivine lattice to the Mg content in atoms per formula unit (apfu, also known as atomic proportion

Endmember Olivine	**d_{130} (Å)**	***a* (Å)**	***b* (Å)**	***c* (Å)**	**Volume (Å^3)**	**Data Points**
Forsterite (Mg_2SiO_4)	2.76529 ± 0.00129	4.75421 ± 0.00215	10.1981 ± 0.0054	5.98131 ± 0.00264	290.000 ± 0.325	23
Fayalite (Fe_2SiO_4)	2.82816 ± 0.00145	4.81925 ± 0.00221	10.4786 ± 0.0074	6.09030 ± 0.00594	307.547 ± 0.489	12
Liebenbergite (Ni_2SiO_4)	2.74603 ± 0.00136	4.72843 ± 0.00262	10.1205 ± 0.0033	5.91295 ± 0.00265	282.958 ± 0.350	6

Table 1. Averaged cell parameters, d_{130} lattice spacing, and volume for the endmember olivine samples.

per formula unit) for both solid solutions. This value is equivalent to 2Mg/(Mg+Fe+Mn+Ni+other trace or major substituted cations) for both Fo-Lbb and Fo-Fa. Discussions of the effects and implications of cation substitution into these solid solutions are also included. This work may be used to determine the composition of olivine on earth and beyond[151, 154-158] relatively quickly, approximately one hour after receiving the sample, by powder XRD and therefore be used for exploration and evaluation of resources targeted for carbon mineralization and critical mineral recovery.

METHODS AND MATERIALS

Data Compilation and Curation. Data compilation began with extracting crystallographic parameters and chemical compositions from within the ICDD powder diffraction database (PDF-4+ 2023). Each data point was added into an excel spreadsheet to curate and remove obvious duplicates from within the data. Duplicates were observed when data from the same study was reported twice, or with slightly different chemical composition data that did not correlate to the literature source. Data was then plotted to pinpoint outliers within the set, and these were then re-checked in the database and literature to determine if the problem point was a result of scan quality or an incorrect or simplified reporting of chemical composition. Outliers were always explained by either of these two factors and were either corrected upon examination of the original literature or removed from the dataset. Approximately 7% of the original dataset

Study	Number of Data Points Used
This Study	162
Morrison et al. (2018)[1]	60
Schwab and Kustner (1977)[2]	23
Jahanbagloo (1969)[3]	16
Louisnathan and Smith (1968)[4]	25
Yoder and Sahama (1957)[5]	31

Table 2: Comparison of data used between current study and previous studies focused on structure-composition relationships between the unit cell parameters and/or lattice plane spacings and the cation composition in Fo-Fa Olivine.

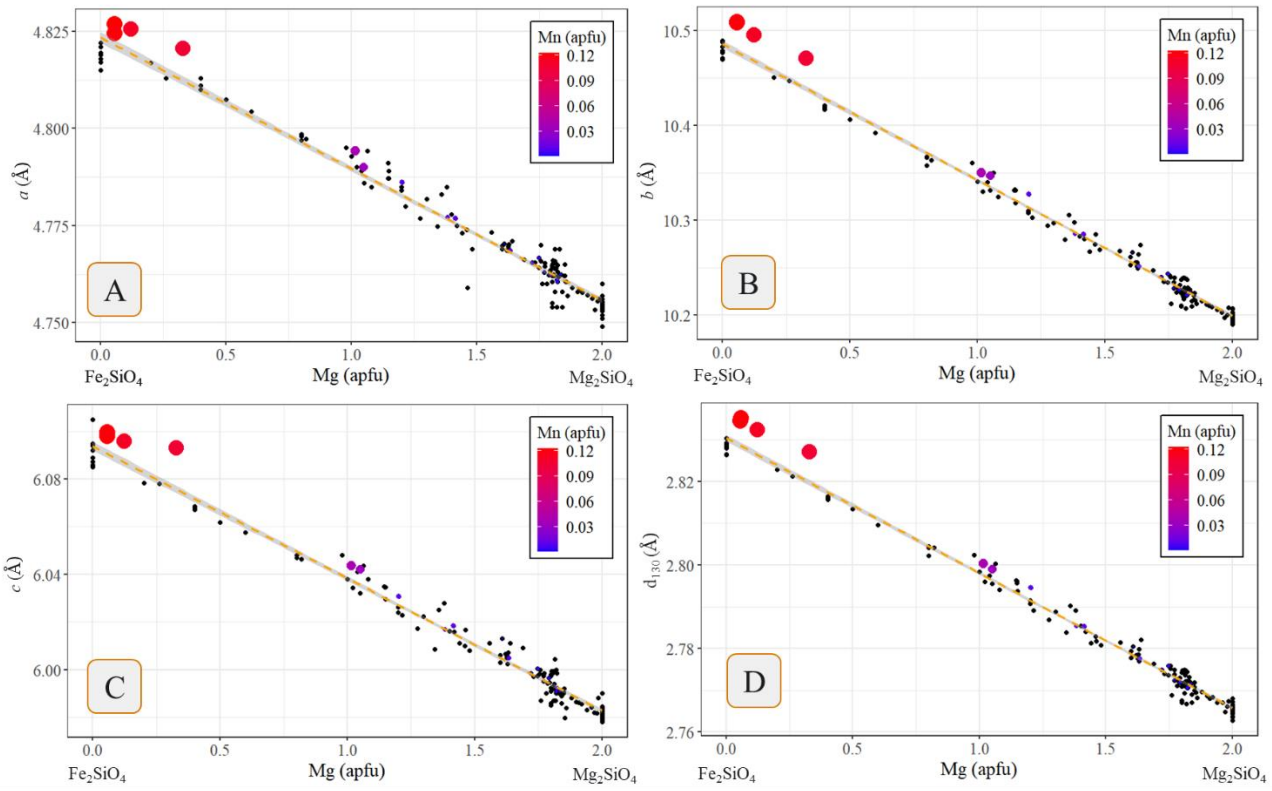

Figure 3: Forsterite – Fayalite cell parameters *a* (A), *b* (B), *c* (C) and d_{130} lattice spacing (D) vs Mg content (apfu). Points are colored and sized by Mn atoms per formula unit. Black points are samples with no reported Mn. Lines of best fit (orange dashes) are plotted and surrounded by a grey 95% confidence interval. The equations for the lines of best fit are reported in top half of Table 3.

Cell Parameters and d_{130}	**Structure-Composition Equation for Fo-Fa with Substituted Cations**	**RMSE**
a (Å)	Mg = -28.7153*a* + 138.547	0.10
b (Å)	Mg = -6.89415*b* + 72.3078	0.065
c (Å)	Mg = -17.6449*c* + 107.554	0.087
d_{130} (Å)	Mg = -30.5803d_{130} + 86.5706	0.068
Cell Parameters and d_{130}	**Structure-Composition Equation for Fo-Fa without Substituted Cations**	**RMSE**
a (Å)	Mg = -29.4019*a* + 141.815	0.095
b (Å)	Mg = -7.07575*b* + 74.1607	0.052
c (Å)	Mg = -18.0860*c* + 110.191	0.077
d_{130} (Å)	Mg = -31.3466d_{130} + 88.6910	0.057

Table 3: Structure-composition equations and RMSE for Fo-Fa olivine with and without substituted cations. The first half of the table uses 162 data points, and the second half uses 131 data points.

was either removed or edited to reflect their literature source.

Plotting and Analysis Methods. The chemical impurity outliers informed a new method of plotting structure composition relationships. This includes plotting a third variable in a two dimensional plot in the programming language R, using the *ggplot2* package[159], with different color and sized points based on the amount of the impurity. This approach allows for outliers to be easily observed and explained and creates new ways to view the structure-compositional relationships of olivine not directly on the solid solution line. Beyond this plotting technique, we modified the R code from Morrison et al.[151] to perform a linear least-squares regression calculation for a line of best fit between the unit cell parameters and d_{130} diffraction peak against the Mg composition for both Fo-Fa and Fo-Lbb olivine. This was then used to calculate a root mean squared error (RMSE) for the line of best fit. Finally, we removed all non-end member olivine with reported trace and major substituted cations (e.g. Co, Mn, Fe, etc.) to recalculate the equations and the RMSE for each of the solid solutions that had no reported impurities. A combination of the two solid solutions was also plotted in a ternary plot, using the *ggtern* package[160] in R.

RESULTS AND DISCUSSION

Olivine Structure-Composition Dataset Characteristics. This study uses 217 data points[132-136, 139, 148, 150, 161-218]; 162 fall into the Fo-Fa solid solution and 78 are Lbb-Fo olivine, with each set sharing the endmember forsterite samples. For endmember olivines, our dataset contains 23 Fo, 12 Fa, and six Lbb samples. The averaged cell parameters, volumes, and d_{130} lattice spacings for Fo, Fa, and Lbb are presented in **Table 1** and all collected literature data is attached as a **Supporting Information** spreadsheet. **Table 2** compares this study to previous studies that created an equation on the structure-composition relationships between the unit cell parameters and/or lattice plane spacings from XRD data and the cation composition of the Fo-Fa series. There have also been other studies that have focused on creating structure composition relationships for olivine by comparing the same structural parameters gathered from XRD but instead of cation composition, created relationships with the mean cation radius[219, 220]. Furthermore, other works have explored structure-composition relationships for Fe-Mn[221], Mg-Mn[221-224], Mg-Mn-Zn[224], Mg-Zn, and Mg-Co[223] olivine. The current dataset compiles over double the XRD scans from the next highest study on Fo-Fa olivine[151], contains more than the combined total of all the major studies listed in **Table 2**, and introduces at least 90 new data points. The composition of both the Fo-Fa and Fo-Lbb series are shown in the ternary plot of **Figure 2**. The vertices of the plot show Fo, Fa, and Lbb and the points are both colored and sized based on the most common

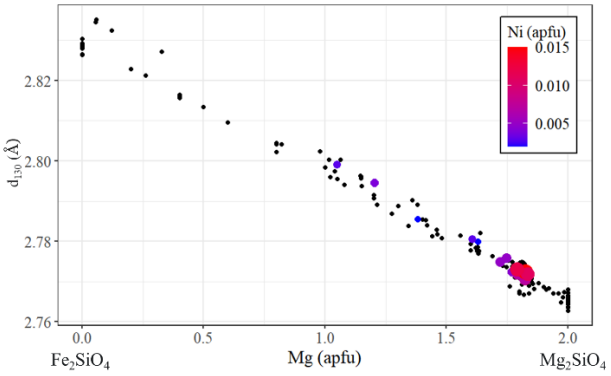

Figure 4: Olivine d_{130} lattice spacing vs Mg content for the Fo-Fa solid solution. Points are colored and sized by Ni content (apfu). Black points contain no reported Ni.

substituted cation in the series, Mn. Most data points are grouped in the Fo-Fa series compared to Fo-Lbb and 101 of the 162 Fo-Fa samples are above Fo_{80}. Additionally, in the Fo-Fa series, 31 non-endmember points contain trace and major substituted cations (Mn, Ni, Co, Cr, Ca), and the Fo-Lbb series contains five points with trace and major substituted cations (Fe, Co), however it is likely not every sample had the exact composition reported, and therefore some reported chemical formulas may be overly simplified.

Forsterite-Fayalite (Mg_2SiO_4 – Fe_2SiO_4). In **Figure 3** there are clear, linear trends for all the cell parameters and d_{130} lattice spacings against the Mg composition of the Fo-Fa olivine samples. The equations for these lines are reported in the top half of **Table 3**, along with the RMSE associated with each. The lowest RMSE is associated with the *b* cell parameter. The bottom half of **Table 3** shows new equations for the solid solution, disregarding any points that contain substituted cations, lowering the associated RMSE, as the effect of cations that are not Fe or Mg tends to move the sample off the linear best fit line.

The plots in **Figure 3** demonstrate the effect that Mn, which was the most abundant trace and major substituted cation in the Fo-Fa series, has on the positioning of points in relation to the overall line of best fit for the data. Since Mn^{2+} is larger than both Fe^{2+} and Mg^{2+}, it increases the cell parameters and d_{130} lattice spacing, as shown. Mn^{2+} is much closer to Fe^{2+} in size than Mg^{2+}, and since it tends to substitute more often into fayalite[149], it has a minimal effect on the series in comparison to the effect of Fe on the Fo-Lbb series. **Figure 3** shows that even at 0.12 apfu Mn, the points are still close to the lines of best fit.

Additionally, in **Figure 4**, we show the inclusion of substituted Ni in the Fo-Fa series. In accordance with previous studies[131, 149], substituted Ni increases with Mg and decreases with Fe. This result has implications for critical mineral exploration and recovery, as the discovery and identification of Mg-rich olivine with

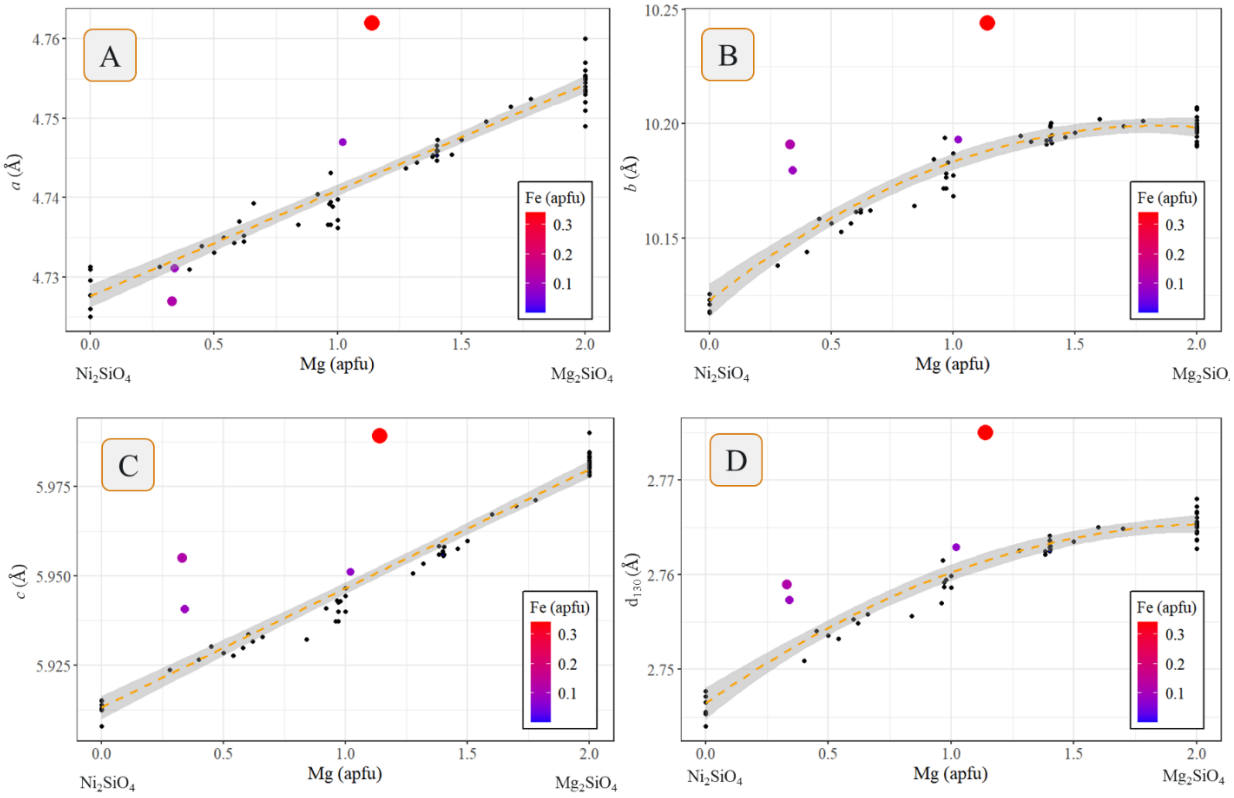

Figure 5: Forsterite – Liebenbergite cell parameters *a* (A), *b* (B), *c* (C) and d_{130} lattice spacing (D) vs Mg content (apfu). Points are colored and sized by Fe atoms per formula unit. Black points are samples with no reported Fe. Lines of best fit (orange dashes) are plotted and surrounded by a grey 95% confidence interval. The equations for the lines of best fit are reported in the top half Table 4.

Cell Parameters and d_{130}	Structure-Composition Equation for Fo-Lbb with Substituted Cations	RMSE
a (Å)	Mg = 5.48098*a* + 1.20635	0.21
b (Å)	Mg = -0.285163b^2 + 4.86330*b* + 1.20635	0.36
c (Å)	Mg = 5.54337*c* + 1.20635	0.19
d_{130} (Å)	Mg = -0.149705d_{130}^2 + 5.02253d_{130} + 1.22550	0.30
Cell Parameters and d_{130}	**Structure-Composition Equations for Fo-Lbb without Substituted Cations**	**RMSE**
a (Å)	Mg = 5.52081*a* + 1.23103	0.14
b (Å)	Mg = 0.974201b^2 + 5.18762*b* + 0.974201	0.24
c (Å)	Mg = 5.60686*c* + 1.23103	0.085
d_{130} (Å)	Mg = 0.897342 d_{130}^2 + 5.23193 d_{130} + 1.25469	0.17

Table 4: Structure-composition equations and RMSE for Fo-Lbb olivine with and without substituted cations. The top half of the data uses 78 data points, and the bottom half uses 73 data points. For d_{130}, the top half uses 70 points and the bottom half uses 65 points.

XRD and other tools likely indicates elevated Ni concentrations. Even ppm levels of Ni within the olivine structure, which would be deemed uneconomical for traditional critical metal mining, may provide a significant source of revue for commercial carbon storage and critical mineral recovery operations when recovered at a large enough scale[121].

Forsterite – Liebenbergite (Mg_2SiO_4 – Ni_2SiO_4). In **Figure 5**, there are again clear trends for d_{130} lattice spacing and the cell parameters against the Mg composition in the series. The top half of **Table 4** presents the equations associated with the lines of best fit in **Figure 5**. The associated RMSE with these points is high, with each equation being above 0.19. This is due in large part to the presence of substituted cations, with the most impactful being Fe^{2+}. Iron causes an increase in cell parameters and d_{130} lattice spacing since it has a much larger cationic size compared to both Ni^{2+} and Mg^{2+}. Thus, when points that only contain Mg and Ni are plotted, the RMSE drops substantially, seen in the bottom half of **Table 3**, with the equation for the *c* cell parameter only having an RMSE of 0.085.

A noticeable difference in **Figure 5B** compared to **Figure 3B** is the quadratic line of best fit for the *b* cell parameter and d_{130} lattice spacing plots. Previous studies[132, 136], also noted the quadratic fit associated with the *b* cell parameter in Mg-Ni olivine. They indicated that the plateau or maximum at Ni amounts less than ~0.5 apfu and is likely associated with a crystal chemistry discontinuity related to Ni's preference to occupy the M1 cation site, which has recently been supported by density functional theory ab initio molecular dynamic calculations[225], and the *b* cell parameter's dependence upon the disorder between the M1 and M2 sites in olivine. The same quadratic trend is observed in this study with the addition of the d_{130} lattice spacing in **Figure 5D**, indicating a similar mechanism causing this plateau for 0-0.5 apfu Ni content in the series. Other studies observed similar non-linearity for the *b* cell parameter in the Mg-Mn[224] and Mg-Co[223] olivine series. Additionally, Lumpkin et al (1983) notes that for Francis (1980), who looked at Mg-Mn olivine, it may be possible to fit the non-linear data with two straight lines[226].

The low-Ni olivine content discontinuity in the Fo-Lbb series also manifests itself in plots of unit cell volume against the cell parameters. **Figure 6** plots the *a*, *b*, and *c* cell parameters, against the unit cell volume for both the Fo-Lbb and Fo-Fa. **Figure 6A**, which plots the *a* cell parameter shows how the slope remains almost constant from Lbb to Fo to Fa, as the slope for Fo-Lbb is 263 and the slope of Fo-Fa is 239. In contrast, **Figure 6B** plots the *b* cell parameter, which is linear for the Fo-Fa series, but when it crosses over to the Fo-Lbb series, we again see a divergence from linearity for low Ni content, which manifests as an effect on the volume of the unit cell. The mechanism for this effect is due to the *b* cell parameter being highly dependent on the size of the M2 cation[219], and since Ni is preferentially occupying the M1 site, the *b* cell parameter remains constant. **Figure 6C,** which plots the *c* cell parameter shows another scenario where, when the two solid solutions meet at Fo, they merely change slope, but both maintain a linear character. The slope of Fo-Lbb is 99 and the slope of Fo-Fa is 161, so there is a clear distinction between the two.

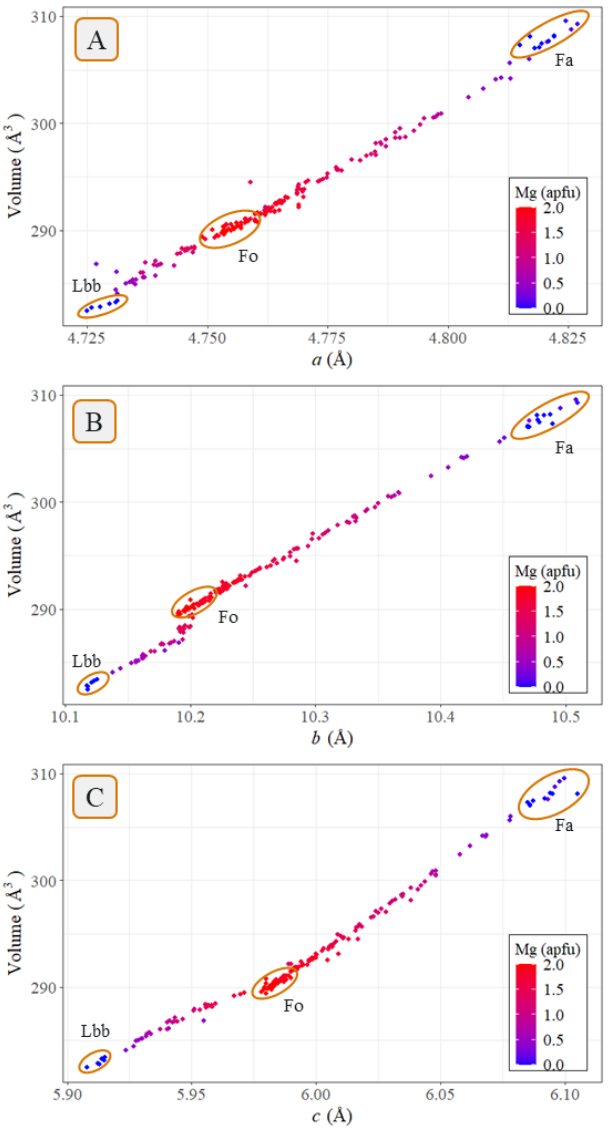

Figure 6: Cell parameters *a* (A), *b* (B), and *c* (C) vs unit cell volume for Lbb-Fo-Fa solid solution. Points are colored by Mg content (apfu). Endmember olivine compositions are circled in orange for reference.

This preference for Ni partitioning into the M1 cation site has potential implications for critical mineral release via olivine dissolution. Preferential olivine dissolution occurs along specific crystallographic planes[22, 227-231] which have different exposures of M1 sites. For instance, Awad[228] et al. demonstrated fastest dissolution rates along the *b* crystallographic axis, where M1 sites are prevalent. However, subsequent work showed dissolution rate variability along the same surfaces and that the primary control on anisotropic dissolution is the number of surface defects, regardless of crystallographic orientation[229]. To the best of our knowledge, the propensity for defects to form on specific olivine surfaces is not yet constrained[232], so the first order controls on anisotropic olivine dissolution is still an open question.

CONCLUSION

Herein we present equations with the ability to predict the chemical composition of Mg-Fe and Mg-Ni olivine sample based on only XRD data and Rietveld refinement analysis. Previous studies largely focused on endmember examples without considering the common substitutions of minor elements for Mg and Fe. By expanding our dataset to include a variety of olivine compositions, both with and without cation substitutions, we provide equations that are more realistic in terms of the estimation and error inherent with calculating composition based on diffraction data. Additionally, we present the structural anomaly present in Fo-Lbb olivine, which results in a quadratic structure-composition equation, in contrast with the linear relationship present in Fo-Fa olivine. These quantitative structure-composition relationship results for the Ni-Mg-Fe olivine ternary will help inform predictive understanding of doping (metal substitution) and reactivity studies given the technologic and environmental importance of olivine. Our results also have potential to enhance exploration and evaluation of assets for olivine-based carbon storage and critical mineral recovery, two linked technologies that may play an important role in the transition to renewable energy.

ASSOCIATED CONTENT

Supporting Information. Reference data for lattice parameters, d-spacings, and olivine compositions. This material is available free of charge on the ACS Publications website at **http://pubs.acs.org**.

AUTHOR INFORMATION

Corresponding Authors
*Corresponding Authors
C. Heath Stanfield, charles.stanfield@pnnl.gov
Quin R.S. Miller, quin.miller@pnnl.gov

Notes
The authors declare no competing financial interests.

ACKNOWLEDGEMENTS

This work was performed at the Pacific Northwest National Laboratory (PNNL) with support from Doug Wicks (DOE HQ) and the DOE Advanced Research Projects Agency-Energy (ARPA-e) MINER program

under contract No. 22/CJ000/09/02. We also acknowledge support from Darin Damiani (DOE HQ) and the U.S. Department of Energy, Office of Fossil Energy and Carbon Management (FECM) through its Carbon Storage program. This work was supported in part by the U.S. Department of Energy, Office of Science, Office of Workforce Development for Teachers and Scientists (WDTS) under the Community College Internships (CCI) program. This work was supported in part by the U.S. Department of Energy, Office of Science, Office of Workforce Development for Teachers and Scientists (WDTS) under the Science Undergraduate Laboratory Internships Program (SULI). This work was supported in part by U.S. Department of Energy, Office of Fossil Energy and Carbon Management Mickey Leland Energy Fellowship (MLEF). AMM (CCI), CHS (SULI), MAM (MLEF), and MFB (SULI) thank the DOE for supporting their internships at PNNL. We thank the two reviewers, including Dr. Roberta Flemming, for their thorough and insightful feedback which greatly improved this study. We also thank Michael C. Perkins (PNNL) for his assistance with graphics support. PNNL is operated by Battelle for the Department of Energy under contract no. DE-AC05-76RLO1830.

REFERENCES

(1) Momma, K.; Izumi, F. VESTA 3 for three-dimensional visualization of crystal, volumetric and morphology data. *Journal of Applied Crystallography* **2011**, *44* (6), 1272-1276. DOI: doi:10.1107/S0021889811038970.

(2) Welsch, B.; First, E. C.; Ruprecht, P.; Jollands, M. C. Olivine—the little green science machine. *Elements* **2023**, *19* (3), 138-143.

(3) Hirth, G.; Kohlstedt, D. Rheology of the Upper Mantle and the Mantle Wedge: A View from the Experimentalists. *Geophysical Monograph 138* **2003**. DOI: 10.1029/138GM06,doi:10.1029/138GM06,Subduction

10.1029/138GM06,Subduction.

(4) Häkli, T. Silicate nickel and its application to the exploration of nickel ores. *Bulletin of the Geological Society of Finland* **1971**, *43* (2), 247-263.

(5) Li, C.; Naldrett, A. Geology and petrology of the Voisey's Bay intrusion: reaction of olivine with sulfide and silicate liquids. *Lithos* **1999**, *47* (1-2), 1-31.

(6) Lightfoot, P.; Naldrett, A.; Hawkesworth, C. The geology and geochemistry of the Waterfall Gorge section of the Insizwa Complex with particular reference to the origin of the nickel sulfide deposits. *Economic Geology* **1984**, *79* (8), 1857-1879.

(7) Makkonen, H. V.; Mäkinen, J.; Kontoniemi, O. Geochemical discrimination between barren and mineralized intrusions in the Svecofennian (1.9 Ga) Kotalahti Nickel Belt, Finland. *Ore Geology Reviews* **2008**, *33* (1), 101-114.

(8) Barnes, S. J.; Fiorentini, M. L. Komatiite magmas and sulfide nickel deposits: a comparison of variably endowed Archean terranes. *Economic Geology* **2012**, *107* (5), 755-780.

(9) Le Vaillant, M.; Barnes, S. J.; Fiorentini, M. L.; Santaguida, F.; Törmänen, T. Effects of hydrous alteration on the distribution of base metals and platinum group elements within the Kevitsa magmatic nickel sulphide deposit. *Ore Geology Reviews* **2016**, *72*, 128-148.

(10) Sobolev, A. V.; Hofmann, A. W.; Sobolev, S. V.; Nikogosian, I. K. An olivine-free mantle source of Hawaiian shield basalts. *Nature* **2005**, *434* (7033), 590-597. DOI: 10.1038/nature03411.

(11) Sobolev, A. V.; Hofmann, A. W.; Kuzmin, D. V.; Yaxley, G. M.; Arndt, N. T.; Chung, S.-L.; Danyushevsky, L. V.; Elliott, T.; Frey, F. A.; Garcia, M. O. The amount of recycled crust in sources of mantle-derived melts. *science* **2007**, *316* (5823), 412-417.

(12) Li, C.; Ripley, E. M. The relative effects of composition and temperature on olivine-liquid Ni partitioning: Statistical deconvolution and implications for petrologic modeling. *Chemical Geology* **2010**, *275* (1-2), 99-104.

(13) Rui, X.; Zhao, X.; Lu, Z.; Tan, H.; Sim, D.; Hng, H. H.; Yazami, R.; Lim, T. M.; Yan, Q. Olivine-type nanosheets for lithium ion battery cathodes. *Acs Nano* **2013**, *7* (6), 5637-5646.

(14) Sun, X.; Tripathi, R.; Popov, G.; Balasubramanian, M.; Nazar, L. F. Stabilization of Lithium Transition Metal Silicates in the Olivine Structure. *Inorganic Chemistry* **2017**, *56* (16), 9931-9937. DOI: 10.1021/acs.inorgchem.7b01453.

(15) Torres, A.; Arroyo-de Dompablo, M. E. Comparative Investigation of MgMnSiO4 and Olivine-Type MgMnSiS4 as Cathode Materials for Mg Batteries. *The Journal of Physical Chemistry C* **2018**, *122* (17), 9356-9362. DOI: 10.1021/acs.jpcc.8b02369.

(16) Shan, P.; Gu, Y.; Yang, L.; Liu, T.; Zheng, J.; Pan, F. Olivine FePO4 Cathode Material for Rechargeable Mg-Ion Batteries. *Inorganic Chemistry* **2017**, *56* (21), 13411-13416. DOI: 10.1021/acs.inorgchem.7b02150.

(17) Sarkar, T.; Bharadwaj, M. D.; Waghmare, U. V.; Kumar, P. Mechanism of Charge Transfer in Olivine-Type LiFeSiO4 and LiFe0.5M0.5SiO4 (M = Mg or Al) Cathode Materials: First-Principles Analysis. *The Journal of*

Physical Chemistry C **2015**, *119* (17), 9125-9133. DOI: 10.1021/acs.jpcc.5b01692.

(18) Dai, D.; Whangbo, M. H.; Koo, H. J.; Rocquefelte, X.; Jobic, S.; Villesuzanne, A. Analysis of the Spin Exchange Interactions and the Ordered Magnetic Structures of Lithium Transition Metal Phosphates LiMPO4 (M = Mn, Fe, Co, Ni) with the Olivine Structure. *Inorganic Chemistry* **2005**, *44* (7), 2407-2413. DOI: 10.1021/ic048431w.

(19) Avdeev, M.; Mohamed, Z.; Ling, C. D.; Lu, J.; Tamaru, M.; Yamada, A.; Barpanda, P. Magnetic Structures of NaFePO4 Maricite and Triphylite Polymorphs for Sodium-Ion Batteries. *Inorganic Chemistry* **2013**, *52* (15), 8685-8693. DOI: 10.1021/ic400870x.

(20) Rimstidt, J. D.; Brantley, S. L.; Olsen, A. A. Systematic review of forsterite dissolution rate data. *Geochimica et Cosmochimica Acta* **2012**, *99*, 159-178. DOI: 10.1016/j.gca.2012.09.019.

(21) Crundwell, F. K. The mechanism of dissolution of forsterite, olivine and minerals of the orthosilicate group. *Hydrometallurgy* **2014**, *150*, 68-82, Article. DOI: 10.1016/j.hydromet.2014.09.006 Scopus.

(22) Oelkers, E. H.; Declercq, J.; Saldi, G. D.; Gislason, S. R.; Schott, J. Olivine dissolution rates: A critical review. *Chemical Geology* **2018**, *500*, 1-19. DOI: https://doi.org/10.1016/j.chemgeo.2018.10.008.

(23) Palandri, J. L.; Kharaka, Y. K. *A compilation of rate parameters of water-mineral interaction kinetics for application to geochemical modeling*; 2004-1068; United States Geological Survey, Menlo Park, California, 2004.

(24) Gerdemann, S. J.; O'Connor, W. K.; Dahlin, D. C.; Penner, L. R.; Rush, H. Ex Situ Aqueous Mineral Carbonation. *Environmental Science & Technology* **2007**, *41* (7), 2587-2593. DOI: 10.1021/es0619253.

(25) Lafay, R.; Montes-Hernandez, G.; Janots, E.; Chiriac, R.; Findling, N.; Toche, F. Simultaneous precipitation of magnesite and lizardite from hydrothermal alteration of olivine under high-carbonate alkalinity. *Chemical Geology* **2014**, *368*, 63-75. DOI: 10.1016/j.chemgeo.2014.01.008.

(26) Jones, L. C.; Rosenbauer, R.; Goldsmith, J. I.; Oze, C. Carbonate control of H_2 and CH_4 production in serpentinization systems at elevated P-Ts. *Geophysical Research Letters* **2010**, *37*, L14306. DOI: 10.1029/2010gl043769.

(27) Klein, F.; McCollom, T. M. From serpentinization to carbonation: New insights from a CO_2 injection experiment. *Earth and Planetary Science Letters* **2013**, *379*, 137-145. DOI: 10.1016/j.epsl.2013.08.017.

(28) Přikryl, J.; Stefánsson, A.; Pearce, C. R. Tracing olivine carbonation and serpentinization in CO_2-rich fluids via magnesium exchange and isotopic fractionation. *Geochimica et Cosmochimica Acta* **2018**, *243*, 133-148. DOI: https://doi.org/10.1016/j.gca.2018.09.022.

(29) Gadikota, G.; Matter, J.; Kelemen, P.; Park, A.-h. A. Chemical and morphological changes during olivine carbonation for CO_2 storage in the presence of NaCl and $NaHCO_3$. *Physical Chemistry Chemical Physics* **2014**, *16* (10), 4679-4693, 10.1039/C3CP54903H. DOI: 10.1039/C3CP54903H.

(30) Eikeland, E.; Blichfeld, A. B.; Tyrsted, C.; Jensen, A.; Iversen, B. B. Optimized carbonation of magnesium silicate mineral for CO_2 storage. *ACS Applied Materials & Interfaces* **2015**, *7* (9), 5258-5264.

(31) Ueda, H.; Sawaki, Y.; Maruyama, S. Reactions between olivine and CO_2-rich seawater at 300 °C: Implications for H_2 generation and CO_2 sequestration on the early Earth. *Geoscience Frontiers* **2017**, *8* (2), 387-396. DOI: 10.1016/j.gsf.2016.10.002.

(32) McCollom, T. M.; Klein, F.; Robbins, M.; Moskowitz, B.; Berquo, T. S.; Jons, N.; Bach, W.; Templeton, A. Temperature trends for reaction rates, hydrogen generation, and partitioning of iron during experimental serpentinization of olivine. *Geochimica et Cosmochimica Acta* **2016**, *181*, 175-200. DOI: 10.1016/j.gca.2016.03.002.

(33) Miller, Q. R. S.; Schaef, H. T.; Kaszuba, J. P.; Qiu, L.; Bowden, M. E.; McGrail, B. P. Tunable Manipulation of Mineral Carbonation Kinetics in Nanoscale Water Films via Citrate Additives. *Environmental Science & Technology* **2018**, *52* (12), 7138-7148. DOI: 10.1021/acs.est.8b00438.

(34) Turri, L.; Muhr, H.; Rijnsburger, K.; Knops, P.; Lapicque, F. CO_2 sequestration by high pressure reaction with olivine in a rocking batch autoclave. *Chemical Engineering Science* **2017**, *171*, 27-31. DOI: https://doi.org/10.1016/j.ces.2017.05.009.

(35) Sekine, Y.; Shibuya, T.; Postberg, F.; Hsu, H. W.; Suzuki, K.; Masaki, Y.; Kuwatani, T.; Mori, M.; Hong, P. K.; Yoshizaki, M.; et al. High-temperature water-rock interactions and hydrothermal environments in the chondrite-like core of Enceladus. *Nature Communications* **2015**, *6*, 8604. DOI: 10.1038/ncomms9604.

(36) Sissmann, O.; Brunet, F.; Martinez, I.; Guyot, F.; Verlaguet, A.; Pinquier, Y.; Daval, D. Enhanced Olivine Carbonation within a Basalt as Compared to Single-Phase Experiments: Reevaluating the Potential of CO_2 Mineral Sequestration. *Environmental Science & Technology* **2014**, *48* (10), 5512-5519. DOI: 10.1021/es405508a (acccessed 2014/05/14).

(37) Miller, Q. R. S.; Kaszuba, J. P.; Schaef, H. T.; Bowden, M. E.; McGrail, B. P.; Rosso, K. M. Anomalously low activation energy of nanoconfined $MgCO_3$ precipitation. *Chemical Communications* **2019**, *55* (48),

6835-6837, 10.1039/C9CC01337G. DOI: 10.1039/C9CC01337G.

(38) Miller, Q. R. S.; Schaef, H. T. Activation energy of magnesite ($MgCO_3$) precipitation: recent insights from olivine carbonation studies. *Environmental Science: Advances* **2022**, *1*, 426-429. DOI: https://doi.org/10.1039/D2VA00066K.

(39) Gadikota, G.; Matter, J.; Kelemen, P.; Brady, P. V.; Park, A.-H. A. Elucidating the differences in the carbon mineralization behaviors of calcium and magnesium bearing alumino-silicates and magnesium silicates for CO2 storage. *Fuel* **2020**, *277*, 117900. DOI: https://doi.org/10.1016/j.fuel.2020.117900.

(40) Sendula, E.; Lamadrid, H. M.; Rimstidt, J. D.; Steele-MacInnis, M.; Sublett, D. M.; Aradi, L. E.; Szabó, C.; Caddick, M. J.; Zajacz, Z.; Bodnar, R. J. Synthetic Fluid Inclusions XXIV. In situ Monitoring of the Carbonation of Olivine Under Conditions Relevant to Carbon Capture and Storage Using Synthetic Fluid Inclusion Micro-Reactors: Determination of Reaction Rates. *Frontiers in Climate* **2021**, *3* (134), 722447, Original Research. DOI: 10.3389/fclim.2021.722447.

(41) Wang, F.; Dreisinger, D.; Jarvis, M.; Hitchins, T. Kinetic evaluation of mineral carbonation of natural silicate samples. *Chemical Engineering Journal* **2021**, *404*, 126522. DOI: https://doi.org/10.1016/j.cej.2020.126522.

(42) Xing, T.; Zhu, W.; Fusseis, F.; Lisabeth, H. Generating porosity during olivine carbonation via dissolution channels and expansion cracks. *Solid Earth* **2018**, *9* (4), 879–896.

(43) Wells, R. K.; Xiong, W.; Sesti, E.; Cui, J.; Giammar, D.; Skemer, P.; Hayes, S. E.; Conradi, M. S. Spatially-variable carbonation reactions in polycrystalline olivine. *Geochimica et Cosmochimica Acta* **2017**, *204*, 252-266. DOI: http://dx.doi.org/10.1016/j.gca.2017.02.003.

(44) Saldi, G. D.; Daval, D.; Guo, H.; Guyot, F.; Bernard, S.; Le Guillou, C.; Davis, J. A.; Knauss, K. G. Mineralogical evolution of Fe-Si-rich layers at the olivine-water interface during carbonation reactions. *American Mineralogist* **2015**, *100* (11-12), 2655-2669. DOI: 10.2138/am-2015-5340.

(45) Johnson, N. C.; Thomas, B.; Maher, K.; Rosenbauer, R. J.; Bird, D.; Brown, G. E., Jr. Olivine dissolution and carbonation under conditions relevant for in situ carbon storage. *Chemical Geology* **2014**, *373*, 93-105. DOI: 10.1016/j.chemgeo.2014.02.026.

(46) Olsson, J.; Bovet, N.; Makovicky, E.; Bechgaard, K.; Balogh, Z.; Stipp, S. L. S. Olivine reactivity with CO2 and H2O on a microscale: Implications for carbon sequestration. *Geochimica Et Cosmochimica Acta* **2012**, *77*, 86-97, Article. DOI: 10.1016/j.gca.2011.11.001.

(47) Hovelmann, J.; Austrheim, H.; Jamtveit, B. Microstructure and porosity evolution during experimental carbonation of a natural peridotite. *Chemical Geology* **2012**, *334*, 254-265, Article. DOI: 10.1016/j.chemgeo.2012.10.025.

(48) King, H. E.; Plumper, O.; Putnis, A. Effect of Secondary Phase Formation on the Carbonation of Olivine. *Environmental Science & Technology* **2010**, *44* (16), 6503-6509. DOI: 10.1021/es9038193.

(49) Prigiobbe, V.; Hänchen, M.; Werner, M.; Baciocchi, R.; Mazzotti, M. Mineral carbonation process for CO2 sequestration. *Energy Procedia* **2009**, *1* (1), 4885.

(50) Bearat, H.; McKelvy, M. J.; Chizmeshya, A. V. G.; Gormley, D.; Nunez, R.; Carpenter, R. W.; Squires, K.; Wolf, G. H. Carbon sequestration via aqueous olivine mineral carbonation: Role of passivating layer formation. *Environmental Science & Technology* **2006**, *40* (15), 4802-4808. DOI: 10.1021/es0523340.

(51) Xiong, W.; Wells, R. K.; Giammar, D. E. Carbon Sequestration in Olivine and Basalt Powder Packed Beds. *Environmental Science & Technology* **2017**, *51* (4), 2105-2112. DOI: 10.1021/acs.est.6b05011.

(52) Adeoye, J. T.; Menefee, A. H.; Xiong, W.; Wells, R. K.; Skemer, P.; Giammar, D. E.; Ellis, B. R. Effect of transport limitations and fluid properties on reaction products in fractures of unaltered and serpentinized basalt exposed to high PCO2 fluids. *International Journal of Greenhouse Gas Control* **2017**, *63*, 310-320. DOI: https://doi.org/10.1016/j.ijggc.2017.06.003.

(53) Menefee, A. H.; Ellis, B. R. Carbon Mineralization in Reactive Silicate Zones. *ACS ES&T Engineering* **2021**, *1* (8), 1193-1204. DOI: 10.1021/acsestengg.1c00066.

(54) Giammar, D. E.; Bruant, R. G.; Peters, C. A. Forsterite dissolution and magnesite precipitation at conditions relevant for deep saline aquifer storage and sequestration of carbon dioxide. *Chemical Geology* **2005**, *217* (3-4), 257-276. DOI: 10.1016/j.chemgeo.2004.12.013.

(55) Miller, Q. R. S.; Schaef, H. T.; Kaszuba, J. P.; Gadikota, G.; McGrail, B. P.; Rosso, K. M. Quantitative Review of Olivine Carbonation Kinetics: Reactivity Trends, Mechanistic Insights, and Research Frontiers. *Environmental Science & Technology Letters* **2019**, *6* (8), 431-442. DOI: 10.1021/acs.estlett.9b00301.

(56) Zare, S.; Funk, A.; Abdolhosseini Qomi, M. J. Formation and Dissolution of Surface Metal Carbonate Complexes: Implications for Interfacial Carbon Mineralization in Metal Silicates. *The Journal of Physical Chemistry C* **2022**, *126* (28), 11574-11584. DOI: 10.1021/acs.jpcc.2c02981.

(57) Zare, S.; Uddin, K. M. S.; Funk, A.; Miller, Q. R. S.; Abdolhosseini Qomi, M. J. Nanoconfinement matters in

humidified CO_2 interaction with metal silicates. *Environmental Science: Nano* **2022**, *9* (10), 3766-3779, 10.1039/D2EN00148A. DOI: 10.1039/D2EN00148A.

(58) Zare, S.; Qomi, M. J. A. Reactive force fields for aqueous and interfacial magnesium carbonate formation. *Physical Chemistry Chemical Physics* **2021**, *23* (40), 23106-23123, 10.1039/D1CP02627E. DOI: 10.1039/D1CP02627E.

(59) Placencia-Gómez, E.; Kerisit, S. N.; Mehta, H. S.; Qafoku, O.; Thompson, C. J.; Graham, T. R.; Ilton, E. S.; Loring, J. S. Critical Water Coverage during Forsterite Carbonation in Thin Water Films: Activating Dissolution and Mass Transport. *Environmental Science & Technology* **2020**, *54* (11), 6888-6899. DOI: 10.1021/acs.est.0c00897.

(60) Kerisit, S. N.; Mergelsberg, S. T.; Thompson, C. J.; White, S. K.; Loring, J. S. Thin Water Films Enable Low-Temperature Magnesite Growth Under Conditions Relevant to Geologic Carbon Sequestration. *Environmental Science & Technology* **2021**, *55* (18), 12539-12548. DOI: 10.1021/acs.est.1c03370.

(61) Mergelsberg, S. T.; Kerisit, S. N.; Ilton, E. S.; Qafoku, O.; Thompson, C. J.; Loring, J. S. Low temperature and limited water activity reveal a pathway to magnesite via amorphous magnesium carbonate. *Chemical Communications* **2020**, *56* (81), 12154-12157, 10.1039/D0CC04907G. DOI: 10.1039/D0CC04907G.

(62) Mergelsberg, S. T.; Rajan, B. P.; Legg, B. A.; Kovarik, L.; Burton, S. D.; Bowers, G. M.; Bowden, M. E.; Qafoku, O.; Thompson, C. J.; Kerisit, S. N.; et al. Nanoscale Mg-Depleted Layers Slow Carbonation of Forsterite (Mg2SiO4) When Water Is Limited. *Environmental Science & Technology Letters* **2023**, *10* (1), 98-104. DOI: 10.1021/acs.estlett.2c00866.

(63) Loring, J. S.; Chen, J.; Benezeth, P.; Qafoku, O.; Ilton, E. S.; Washton, N. M.; Thompson, C. J.; Martin, P. F.; McGrail, B. P.; Rosso, K. M.; et al. Evidence for carbonate surface complexation during forsterite carbonation in wet supercritical carbon dioxide. *Langmuir* **2015**, *31* (27), 7533-7543. DOI: 10.1021/acs.langmuir.5b01052.

(64) Miller, Q. R. S.; Kaszuba, J. P.; Schaef, H. T.; Bowden, M. E.; McGrail, B. P. Impacts of organic ligands on forsterite reactivity in supercritical CO_2 fluids. *Environmental Science & Technology* **2015**, *49* (7), 4724-4734. DOI: 10.1021/es506065d.

(65) Thompson, C. J.; Martin, P. F.; Chen, J.; Benezeth, P.; Schaef, H. T.; Rosso, K. M.; Felmy, A. R.; Loring, J. S. Automated high-pressure titration system with in situ infrared spectroscopic detection. *Review of Scientific Instruments* **2014**, *85* (4), 044102. DOI: 10.1063/1.4870411.

(66) Miller, Q. R. S.; Kaszuba, J. P.; Kerisit, S. N.; Schaef, H. T.; Bowden, M. E.; McGrail, B. P.; Rosso, K. M. Emerging investigator series: ion diffusivities in nanoconfined interfacial water films contribute to mineral carbonation thresholds. *Environmental Science: Nano* **2020**, *7* (4), 1068-1081, 10.1039/C9EN01382B. DOI: 10.1039/C9EN01382B.

(67) Felmy, A. R.; Qafoku, O.; Arey, B. W.; Hu, J. Z.; Hu, M.; Todd Schaef, H.; Ilton, E. S.; Hess, N. J.; Pearce, C. I.; Feng, J.; et al. Reaction of water-saturated supercritical CO_2 with forsterite: Evidence for magnesite formation at low temperatures. *Geochimica et Cosmochimica Acta* **2012**, *91*, 271-282. DOI: 10.1016/j.gca.2012.05.026.

(68) Wang, Z.; Felmy, A. R.; Thompson, C. J.; Loring, J. S.; Joly, A. G.; Rosso, K. M.; Schaef, H. T.; Dixon, D. A. Near-infrared spectroscopic investigation of water in supercritical CO_2 and the effect of $CaCl_2$. *Fluid Phase Equilibria* **2013**, *338*, 155-163. DOI: 10.1016/j.fluid.2012.11.012.

(69) Loring, J. S.; Thompson, C. J.; Wang, Z.; Joly, A. G.; Sklarew, D. S.; Schaef, H. T.; Ilton, E. S.; Rosso, K. M.; Felmy, A. R. In Situ Infrared Spectroscopic Study of Forsterite Carbonation in Wet Supercritical CO2. *Environmental Science & Technology* **2011**, *45* (14), 6204-6210. DOI: 10.1021/es201284e.

(70) Qomi, M. J. A.; Miller, Q. R. S.; Zare, S.; Schaef, H. T.; Kaszuba, J. P.; Rosso, K. M. Molecular-Scale Mechanisms of CO_2 Mineralization in Nanoscale Interfacial Water Films. *Nature Reviews Chemistry* **2022**, *6*, 598–613. DOI: https://doi.org/10.1038/s41570-022-00418-1.

(71) Qafoku, O.; Hu, J.; Hess, N. J.; Hu, M. Y.; Ilton, E. S.; Feng, J.; Arey, B. W.; Felmy, A. R. Formation of submicron magnesite during reaction of natural forsterite in H_2O-saturated supercritical CO_2. *Geochimica et Cosmochimica Acta* **2014**, *134*, 197-209. DOI: 10.1016/j.gca.2013.09.024.

(72) Schaef, H. T.; McGrail, B. P.; Loring, J. L.; Bowden, M. E.; Arey, B. W.; Rosso, K. M. Forsterite [Mg_2SiO_4)] Carbonation in Wet Supercritical CO_2: An in Situ High-Pressure X-ray Diffraction Study. *Environmental Science & Technology* **2013**, *47* (1), 174-181. DOI: 10.1021/es301126f.

(73) Miller, Q. R. S.; Dixon, D. A.; Burton, S. D.; Walter, E. D.; Hoyt, D. W.; McNeill, A. S.; Moon, J. D.; Thanthiriwatte, K. S.; Ilton, E. S.; Qafoku, O.; et al. Surface-Catalyzed Oxygen Exchange during Mineral Carbonation in Nanoscale Water Films. *The Journal of Physical Chemistry C* **2019**, *123* (20), 12871-12885. DOI: 10.1021/acs.jpcc.9b02215.

(74) Qafoku, O.; Kovarik, L.; Kukkadapu, R. K.; Ilton, E. S.; Arey, B. W.; Tucek, J.; Felmy, A. R. Fayalite dissolution and siderite formation in water-saturated supercritical CO_2. *Chemical Geology* **2012**, *332*, 124-135, Article. DOI: 10.1016/j.chemgeo.2012.09.028.

(75) Li, X.; Nienhuis, E. T.; Nagurney, A. B.; Miller, Q. R. S.; Zhang, X.; Schaef, H. T. Resolving Nanoscale Processes during Carbon Mineralization Using Identical Location Transmission Electron Microscopy. *Environmental Science & Technology Letters* **2023**. DOI: 10.1021/acs.estlett.3c00699.

(76) O'Connor, W.; Dahlin, D.; Rush, G.; Gerdemann, S.; Penner, L.; Nilsen, D. *Aqueous mineral carbonation: Mineral availability, pretreatment, reaction parametrics, and process studies (DOE/ARC-TR-04-002)*; DOE/ARC-TR-04-002; National Energy Technology Laboratory, Albany, OR, USA, 2005. https://www.netl.doe.gov/File%20Library/Research/Coal/NETLAlbanyAqueousMineralCarbonation.pdf.

(77) Gerdemann, S.; Dahlin, D.; O'Connor, W.; Penner, L. *Carbon dioxide sequestration by aqueous mineral carbonation of magnesium silicate minerals (DOE/ARC-2003-018)*; (DOE/ARC-2003-018); National Energy Technology Laboratory, Albany, OR, USA, 2003. https://www.netl.doe.gov/File%20Library/Research/Coal/NETLAlbanyAqueousMineralCarbonation.pdf.

(78) Chizmeshya, A. V.; McKelvy, M. J.; Squires, K.; Carpenter, R. W.; Bearat, H. *A novel approach to mineral carbonation: Enhancing carbonation while avoiding mineral pretreatment process cost*; Arizona State Univ., Tempe, AZ (United States), 2007.

(79) Lafay, R.; Montes-Hernandez, G.; Renard, F.; Vonlanthen, P. Intracrystalline Reaction-Induced Cracking in Olivine Evidenced by Hydration and Carbonation Experiments. *Minerals* **2018**, *8* (9), 412. DOI: https://doi.org/10.3390/min8090412.

(80) Maher, K.; Johnson, N. C.; Jackson, A.; Lammers, L. N.; Torchinsky, A. B.; Weaver, K. L.; Bird, D. K.; Brown, G. E., Jr. A spatially resolved surface kinetic model for forsterite dissolution. *Geochimica et Cosmochimica Acta* **2016**, *174*, 313-334. DOI: 10.1016/j.gca.2015.11.019.

(81) Wang, F.; Giammar, D. E. Forsterite Dissolution in Saline Water at Elevated Temperature and High CO_2 Pressure *Environ. Sci. Technol.* **2013**, *47* (1), 168-173.

(82) Jarvis, K.; Carpenter, R. W.; Windman, T.; Kim, Y.; Nunez, R.; Alawneh, F. Reaction Mechanisms for Enhancing Mineral Sequestration of CO_2. *Environmental Science & Technology* **2009**, *43* (16), 6314-6319. DOI: 10.1021/es8033507.

(83) Milliken, R. E.; Rivkin, A. S. Brucite and carbonate assemblages from altered olivine-rich materials on Ceres. *Nat. Geosci.* **2009**, *2* (4), 258.

(84) Matter, J. M.; Takahashi, T.; Goldberg, D. Experimental evaluation of in situ CO_2-water-rock reactions during CO_2 injection in basaltic rocks: Implications for geological CO_2 sequestration. *Geochemistry Geophysics Geosystems* **2007**, *8*, Article. DOI: Q02001

10.1029/2006gc001427.

(85) Oelkers, E. H.; Gislason, S. R.; Matter, J. Mineral carbonation of CO_2. *Elements* **2008**, *4* (5), 333-337.

(86) Dufaud, F.; Martinez, I.; Shilobreeva, S. Experimental study of Mg-rich silicates carbonation at 400 and 500 °C and 1 kbar. *Chemical Geology* **2009**, *265* (1-2), 79-87. DOI: 10.1016/j.chemgeo.2009.01.026.

(87) Matter, J. M.; Kelemen, P. B. Permanent storage of carbon dioxide in geological reservoirs by mineral carbonation. *Nature Geoscience* **2009**, *2* (12), 837-841, Article. DOI: 10.1038/ngeo683.

(88) Beinlich, A.; Austrheim, H. In situ sequestration of atmospheric CO2 at low temperature and surface cracking of serpentinized peridotite in mine shafts. *Chemical Geology* **2012**, *332*, 32-44, Article. DOI: 10.1016/j.chemgeo.2012.09.015.

(89) Daval, D.; Sissmann, O.; Menguy, N.; Saldi, G. D.; Guyot, F.; Martinez, I.; Corvisier, J.; Garcia, B.; Machouk, I.; Knauss, K. G.; et al. Influence of amorphous silica layer formation on the dissolution rate of olivine at 90 degrees C and elevated pCO(2). *Chemical Geology* **2011**, *284* (1-2). DOI: 10.1016/j.chemgeo.2011.02.021.

(90) Guyot, F.; Daval, D.; Dupraz, S.; Martinez, I.; Menez, B.; Sissmann, O. CO2 geological storage: The environmental mineralogy perspective. *Comptes Rendus Geoscience* **2011**, *343* (2-3), 246-259. DOI: 10.1016/j.crte.2010.12.007.

(91) Klein, F.; Garrido, C. J. Thermodynamic constraints on mineral carbonation of serpentinized peridotite. *Lithos* **2011**, *126* (3-4), 147-160. DOI: 10.1016/j.lithos.2011.07.020.

(92) Fleury, M.; Kohler, E.; Norrant, F.; Gautier, S.; M'Hamdi, J.; Barre, L. Characterization and Quantification of Water in Smectites with Low-Field NMR. *Journal of Physical Chemistry C* **2013**, *117* (9), 4551-4560. DOI: 10.1021/jp311006q.

(93) Gislason, S. R.; Oelkers, E. H. Carbon Storage in Basalt. *Science* **2014**, *344* (6182), 373-374. DOI: 10.1126/science.1250828.

(94) Zhu, W.; Fusseis, F.; Lisabeth, H.; Xing, T.; Xiao, X.; De Andrade, V.; Karato, S. i. Experimental evidence of reaction-induced fracturing during olivine carbonation. *Geophysical Research Letters* **2016**, *43* (18), 9535-9543.

(95) Li, Q.; Jun, Y.-S. The apparent activation energy and pre-exponential kinetic factor for heterogeneous calcium carbonate nucleation on quartz. *Communications Chemistry* **2018**, *1* (1). DOI: 10.1038/s42004-018-0056-5.

(96) Renforth, P.; Pogge von Strandmann, P. A. E.; Henderson, G. M. The dissolution of olivine added to soil: Implications for enhanced weathering. *Applied Geochemistry* **2015**, *61*, 109-118. DOI: 10.1016/j.apgeochem.2015.05.016.

(97) Hamilton, J. L.; Wilson, S.; Morgan, B.; Harrison, A. L.; Turvey, C. C.; Paterson, D. J.; Dipple, G. M.; Southam, G. Accelerating mineral carbonation in ultramafic mine tailings via direct CO2 reaction and heap leaching with potential for base metal enrichment and recovery. *Economic Geology* **2020**, *115* (2), 303-323.

(98) Hamilton, J. L.; Wilson, S.; Morgan, B.; Turvey, C. C.; Paterson, D. J.; Jowitt, S. M.; McCutcheon, J.; Southam, G. Fate of transition metals during passive carbonation of ultramafic mine tailings via air capture with potential for metal resource recovery. *International Journal of Greenhouse Gas Control* **2018**, *71*, 155-167.

(99) Hamilton, J. L.; Wilson, S. A.; Morgan, B.; Turvey, C. C.; Paterson, D. J.; Jowitt, S. M.; McCutcheon, J.; Southam, G. Fate of transition metals during passive carbonation of ultramafic mine tailings via air capture with potential for metal resource recovery. *International Journal of Greenhouse Gas Control* **2018**, *71*, 155-167. DOI: 10.1016/j.ijggc.2018.02.008.

(100) Kelemen, P. B.; Matter, J.; Streit, E. E.; Rudge, J. F.; Curry, W. B.; Blusztajn, J. Rates and Mechanisms of Mineral Carbonation in Peridotite: Natural Processes and Recipes for Enhanced, in situ CO2 Capture and Storage. In *Annual Review of Earth and Planetary Sciences, Vol 39*, Jeanloz, R., Freeman, K. H. Eds.; Annual Review of Earth and Planetary Sciences, Vol. 39; 2011; pp 545-576.

(101) Peuble, S.; Andreani, M.; Gouze, P.; Pollet-Villard, M.; Reynard, B.; Van de Moortele, B. Multi-scale characterization of the incipient carbonation of peridotite. *Chemical Geology* **2017**.

(102) Kelemen, P. B.; Matter, J. In situ carbonation of peridotite for CO_2 storage. *Proceedings of the National Academy of Science* **2008**, *105* (45), 17295-17300. DOI: 10.1073/pnas.0805794105.

(103) Van Noort, R.; Spiers, C.; Drury, M.; Kandianis, M. Peridotite dissolution and carbonation rates at fracture surfaces under conditions relevant for in situ mineralization of CO2. *Geochimica et Cosmochimica Acta* **2013**, *106*, 1-24.

(104) Hövelmann, J.; Austrheim, H.; Beinlich, A.; Anne Munz, I. Experimental study of the carbonation of partially serpentinized and weathered peridotites. *Geochimica et Cosmochimica Acta* **2011**, *75* (22), 6760-6779. DOI: http://dx.doi.org/10.1016/j.gca.2011.08.032.

(105) Rudge, J. F.; Kelemen, P. B.; Spiegelman, M. A simple model of reaction-induced cracking applied to serpentinization and carbonation of peridotite. *Earth and Planetary Science Letters* **2010**, *291* (1-4), 215-227.

(106) Lacinska, A. M.; Styles, M. T.; Bateman, K.; Hall, M.; Brown, P. An experimental study of the carbonation of serpentinite and partially serpentinised peridotites. *Frontiers in Earth Science* **2017**, *5* (37), 37. DOI: 10.3389/feart.2017.00037.

(107) Grozeva, N. G.; Klein, F.; Seewald, J. S.; Sylva, S. P. Experimental study of carbonate formation in oceanic peridotite. *Geochimica et Cosmochimica Acta* **2017**, *199*, 264-286. DOI: http://dx.doi.org/10.1016/j.gca.2016.10.052.

(108) Menzel, M. D.; Garrido, C. J.; López Sánchez-Vizcaíno, V.; Marchesi, C.; Hidas, K.; Escayola, M. P.; Delgado Huertas, A. Carbonation of mantle peridotite by CO_2-rich fluids: the formation of listvenites in the Advocate ophiolite complex (Newfoundland, Canada). *Lithos* **2018**, *323*, 238-261. DOI: https://doi.org/10.1016/j.lithos.2018.06.001.

(109) Rahmani, O.; Highfield, J.; Junin, R.; Tyrer, M.; Pour, A. B. Experimental investigation and simplistic geochemical modeling of CO2 mineral carbonation using the mount tawai peridotite. *Molecules* **2016**, *21* (3), 353.

(110) Mervine, E. M.; Humphris, S. E.; Sims, K. W. W.; Kelemen, P. B.; Jenkins, W. J. Carbonation rates of peridotite in the Samail Ophiolite, Sultanate of Oman, constrained through 14C dating and stable isotopes. *Geochimica et Cosmochimica Acta* **2014**, *126*, 371-397.

(111) Paukert, A. N.; Matter, J. M.; Kelemen, P. B.; Shock, E. L.; Havig, J. R. Reaction path modeling of enhanced in situ CO2 mineralization for carbon sequestration in the peridotite of the Samail Ophiolite, Sultanate of Oman. *Chemical Geology* **2012**, *330*, 86-100. DOI: 10.1016/j.chemgeo.2012.08.013.

(112) Decrausaz, T.; Godard, M.; Menzel, M. D.; Parat, F.; Oliot, E.; Lafay, R.; Barou, F. Pervasive carbonation of peridotite to listvenite (Semail Ophiolite, Sultanate of Oman): clues from iron partitioning and chemical zoning. *European Journal of Mineralogy* **2023**, *35* (2), 171-187.

(113) Andreani, M.; Luquot, L.; Gouze, P.; Godard, M.; Hoise, E.; Gibert, B. Experimental Study of Carbon Sequestration Reactions Controlled by the Percolation of CO_2-Rich Brine through Peridotites. *Environmental Science & Technology* **2009**, *43* (4), 1226-1231. DOI: 10.1021/es8018429.

(114) Rigopoulos, I.; Harrison, A. L.; Delimitis, A.; Ioannou, I.; Efstathiou, A. M.; Kyratsi, T.; Oelkers, E. H. Carbon sequestration via enhanced weathering of peridotites and basalts in seawater. *Applied Geochemistry* **2018**, *91*, 197-207. DOI: 10.1016/j.apgeochem.2017.11.001.

(115) García del Real, P.; Vishal, V. Mineral carbonation in ultramafic and basaltic rocks. *Geologic carbon sequestration: Understanding reservoir behavior* **2016**, 213-229.

(116) Tominaga, M.; Beinlich, A.; Lima, E. A.; Tivey, M. A.; Hampton, B. A.; Weiss, B.; Harigane, Y. Multi-scale magnetic mapping of serpentinite carbonation. *Nature communications* **2017**, *8* (1), 1870.

(117) Kelemen, P. B.; Aines, R.; Bennett, E.; Benson, S. M.; Carter, E.; Coggon, J. A.; De Obeso, J. C.; Evans, O.; Gadikota, G.; Dipple, G. M. In situ carbon mineralization in ultramafic rocks: Natural processes and possible engineered methods. *Energy Procedia* **2018**, *146*, 92-102.

(118) de Obeso, J. C.; Santiago Ramos, D. P.; Higgins, J. A.; Kelemen, P. B. A Mg isotopic perspective on the mobility of magnesium during serpentinization and carbonation of the Oman ophiolite. *Journal of Geophysical Research: Solid Earth* **2021**, *126* (2), e2020JB020237.

(119) Beinlich, A.; Plümper, O.; Boter, E.; Müller, I. A.; Kourim, F.; Ziegler, M.; Harigane, Y.; Lafay, R.; Kelemen, P. B.; Oman Drilling Project Science, T. Ultramafic rock carbonation: Constraints from listvenite core BT1B, Oman Drilling Project. *Journal of Geophysical Research: Solid Earth* **2020**, *125* (6), e2019JB019060.

(120) Okazaki, K.; Michibayashi, K.; Hatakeyama, K.; Abe, N.; Johnson, K. T.; Kelemen, P. B.; Team, O. D. P. S. Major Mineral Fraction and Physical Properties of Carbonated Peridotite (Listvenite) From ICDP Oman Drilling Project Hole BT1B Inferred From X-Ray CT Core Images. *Journal of Geophysical Research: Solid Earth* **2021**, *126* (12), e2021JB022719.

(121) Stanfield, C. H.; Miller, Q. R. S.; Battu, A. K.; Lahiri, N.; Nagurney, A. B.; Cao, R.; Nienhuis, E. T.; DePaolo, D. J.; Latta, D. E.; Schaef, H. T. Carbon Mineralization and Critical Mineral Resource Evaluation Pathways for Mafic–Ultramafic Assets. *ACS Earth and Space Chemistry* **2024**. DOI: 10.1021/acsearthspacechem.4c00005.

(122) Steinthorsdottir, K.; Dipple, G. M.; Cutts, J. A.; Turvey, C. C.; Milidragovic, D.; Peacock, S. M. Formation and Preservation of Brucite and Awaruite in Serpentinized and Tectonized Mantle in Central British Columbia: Implications for Carbon Mineralization and Nickel Mining. *Journal of Petrology* **2022**, *63* (11). DOI: 10.1093/petrology/egac100 (acccessed 9/14/2023).

(123) Wilson, S.; Hamilton, J. L. Fizzy ore processing sequesters CO_2 while supplying critical metals. *Proceedings of the National Academy of Sciences* **2022**, *119* (39), e2212424119. DOI: doi:10.1073/pnas.2212424119.

(124) Santos, R. M.; Van Audenaerde, A.; Chiang, Y. W.; Iacobescu, R. I.; Knops, P.; Van Gerven, T. Nickel extraction from olivine: effect of carbonation pre-treatment. *Metals* **2015**, *5* (3), 1620-1644.

(125) Wang, F.; Dreisinger, D. Carbon mineralization with concurrent critical metal recovery from olivine. *Proceedings of the National Academy of Sciences* **2022**, *119* (32), e2203937119.

(126) Wang, F.; Dreisinger, D. An integrated process of CO2 mineralization and selective nickel and cobalt recovery from olivine and laterites. *Chemical Engineering Journal* **2023**, *451*, 139002. DOI: https://doi.org/10.1016/j.cej.2022.139002.

(127) Wang, F.; Dreisinger, D. Enhanced CO2 mineralization and selective critical metal extraction from olivine and laterites. *Separation and Purification Technology* **2023**, *321*, 124268. DOI: https://doi.org/10.1016/j.seppur.2023.124268.

(128) Wang, F.; Dreisinger, D.; Xiao, Y. Accelerated CO2 mineralization and utilization for selective battery metals recovery from olivine and laterites. *Journal of Cleaner Production* **2023**, *393*, 136345. DOI: https://doi.org/10.1016/j.jclepro.2023.136345.

(129) Nagurney, A.; Lahiri, N.; Murchland, M. A.; Blondes, M. S.; Thakurta, J.; Gadikota, G.; Schaef, H. T. V22A-07: Carbon-negative mining advancements to promote the green energy transition. In AGU Annual Fall Meeting 2023, San Francisco, California; Paper V23B-0164, 2023.

(130) Murchland, M. A.; Nagurney, A. B.; Lahiri, N.; Engelhard, M. H.; Schaef, H. T.; Miller, Q. R. S. V23B-0164: Concurrent Carbon Mineralization and Critical Metal Mobilization in Eagle Intrusion Peridotites. In AGU Annual Fall Meeting 2023, San Francisco, California; Paper V23B-0164, 2023.

(131) Barnes, S. J.; Yao, Z.-S.; Mao, Y.-J.; Jesus, A. P.; Yang, S.; Taranovic, V.; Maier, W. D. Nickel in olivine as an exploration indicator for magmatic Ni-Cu sulfide deposits: A data review and re-evaluation. *American Mineralogist* **2023**, *108* (1), 1-17. DOI: 10.2138/am-2022-8327.

(132) Henderson, C. M. B.; Redfern, S. A.; Smith, R. I.; Knight, K. S.; Charnock, J. M. Composition and temperature dependence of cation ordering in Ni-Mg olivine solid solutions: a time-of-flight neutron powder diffraction and EXAFS study. *American Mineralogist* **2001**, *86* (10), 1170-1187.

(133) Rajmani, V.; Brown, G. E.; Prewitt, C. Cation ordering in Ni-Mg olivine. *American Mineralogist: Journal of Earth and Planetary Materials* **1975**, *60* (3-4), 292-299.

(134) Bish, D. L. Cation ordering in synthetic and natural Ni–Mg olivine. *American Mineralogist* **1981**, *66* (7-8), 770-776.

(135) Ottonello, G.; Della Giusta, A.; Molin, G. Cation ordering in Ni-Mg olivines. *American Mineralogist* **1989**, *74* (3-4), 411-421.

(136) Bostroem, D. Single-crystal X-ray diffraction studies of synthetic Ni-Mg olivine solid solutions. *American Mineralogist* **1987**, *72* (9-10), 965-972.

(137) Tsukimura, K.; Sasaki, S. Determination of cation distribution in (Co, Ni, Zn) 2 SiO 4 olivine by synchrotron X-ray diffraction. *Physics and Chemistry of Minerals* **2000**, *27*, 234-241.

(138) Annersten, H.; Adetunji, J.; Filippidis, A. Cation ordering in Fe–Mn silicate olivines. *American Mineralogist* **1984**, *69* (11-12), 1110-1115.

(139) Nord, A. G.; Annersten, H.; Filippidis, A. The cation distribution in synthetic Mg–Fe–Ni olivines. *American Mineralogist* **1982**, *67* (11-12), 1206-1211.

(140) Casey, W. H.; Westrich, H. R. Control of dissolution rates of orthosilicate minerals by divalent metal–oxygen bonds. *Nature* **1992**, *355*, 157. DOI: 10.1038/355157a0.

(141) IEA. *The Role of Critical Minerals in Clean Energy Transitions*; IEA, Paris, 2021. DOI: https://www.iea.org/reports/the-role-of-critical-minerals-in-clean-energy-transitions.

(142) *The role of critical minerals in clean energy transitions*; International Energy Agency, 2021.

(143) *Minerals for climate action: The mineral intensity of the clean energy transition*; World Bank Group, 2020.

(144) Liu, W.; Oh, P.; Liu, X.; Lee, M. J.; Cho, W.; Chae, S.; Kim, Y.; Cho, J. Nickel-rich layered lithium transition-metal oxide for high-energy lithium-ion batteries. *Angewandte Chemie International Edition* **2015**, *54* (15), 4440-4457.

(145) Taranovic, V.; Ripley, E. M.; Li, C.; Rossell, D. Petrogenesis of the Ni–Cu–PGE sulfide-bearing Tamarack Intrusive Complex, Midcontinent Rift System, Minnesota. *Lithos* **2015**, *212-215*, 16-31. DOI: 10.1016/j.lithos.2014.10.012.

(146) Onyeagocha, A. Twin Sisters dunite: petrology and mineral chemistry. *Geological Society of America Bulletin* **1978**, *89* (10), 1459-1474.

(147) Lambart, S.; Hamilton, S.; Lang, O. I. Compositional variability of San Carlos olivine. *Chemical Geology* **2022**, *605*, 120968. DOI: https://doi.org/10.1016/j.chemgeo.2022.120968.

(148) Francis, C. A. New data on the forsterite–tephroite series. *American Mineralogist* **1985**, *70* (5-6), 568-575.

(149) Simkin, T.; Smith, J. Minor-element distribution in olivine. *The Journal of Geology* **1970**, *78* (3), 304-325.

(150) Schwab, R.; Kustner, D. Precise determination of lattice constants to establish X-ray determinative curves for synthetic olivines of the solid solution series forsterite-fayalite. *Neues Jahrbuch fur Mineralogie Monatshefte* **1977**, *5*, 205-215.

(151) Morrison, S. M.; Downs, R. T.; Blake, D. F.; Prabhu, A.; Eleish, A.; Vaniman, D. T.; Ming, D. W.; Rampe, E. B.; Hazen, R. M.; Achilles, C. N. Relationships between unit-cell parameters and composition for rock-forming minerals on Earth, Mars, and other extraterrestrial bodies. *American Mineralogist* **2018**, *103* (6), 848-856.

(152) Jollands, M. C.; Dohmen, R.; Padrón-Navarta, J. A. Hide and Seek—Trace Element Incorporation and Diffusion in Olivine. *Elements* **2023**, *19* (3), 144-150.

(153) Demouchy, S.; Alard, O. Hydrogen, trace, and ultra-trace element distribution in natural olivines. *Contributions to Mineralogy and Petrology* **2021**, *176* (4), 26.

(154) Di Cecco, V. E.; Hyde, B. C.; Tait, K. T.; Nicklin, R. I. Determination of olivine fayalite–forsterite composition in ordinary chondrites by X-ray diffraction. *Meteoritics & Planetary Science* **2022**, *57* (6), 1288-1299. DOI: https://doi.org/10.1111/maps.13824.

(155) Mustard, J.; Poulet, F.; Gendrin, A.; Bibring, J.-P.; Langevin, Y.; Gondet, B.; Mangold, N.; Bellucci, G.; Altieri, F. Olivine and pyroxene diversity in the crust of Mars. *Science* **2005**, *307* (5715), 1594-1597.

(156) Hoefen, T. M.; Clark, R. N.; Bandfield, J. L.; Smith, M. D.; Pearl, J. C.; Christensen, P. R. Discovery of olivine in the Nili Fossae region of Mars. *Science* **2003**, *302* (5645), 627-630.

(157) Yamamoto, S.; Nakamura, R.; Matsunaga, T.; Ogawa, Y.; Ishihara, Y.; Morota, T.; Hirata, N.; Ohtake, M.; Hiroi, T.; Yokota, Y. Possible mantle origin of olivine around lunar impact basins detected by SELENE. *Nature Geoscience* **2010**, *3* (8), 533-536.

(158) Klöck, W.; Thomas, K.; McKay, D.; Palme, H. Unusual olivine and pyroxene composition in interplanetary dust and unequilibrated ordinary chondrites. *Nature* **1989**, *339* (6220), 126-128.

(159) Wickham, H. *ggplot2: Elegant Graphics for Data Analysis*; Springer-Verlag New York, 2016.

(160) Hamilton, N. E.; Ferry, M. ggtern: Ternary Diagrams Using ggplot2. *Journal of Statistical Software, Code Snippets* **2018**, *87* (3), 1 - 17. DOI: 10.18637/jss.v087.c03 (acccessed 2024/01/17).

(161) Swanson, H. E.; Tatge, E. Standard X-ray diffraction patterns. *Journal of Research of the National Bureau of Standards* **1951**, *46* (4), 318.

(162) Yoder Jr, H.; Sahama, T. G. Olivine X-ray determinative curve. *American Mineralogist: Journal of Earth and Planetary Materials* **1957**, *42* (7-8), 475-491.

(163) Smyth, J. R. High temperature crystal chemistry of fayalite. *American Mineralogist: Journal of Earth and Planetary Materials* **1975**, *60* (11-12), 1092-1097.

(164) Wenk, H.-R.; Raymond, K. Four new structure refinements of olivine. *Zeitschrift für Kristallographie-Crystalline Materials* **1973**, *137* (1-6), 86-105.

(165) Smyth, J. R.; Hazen, R. M. The crystal structures of forsterite and hortonolite at several temperatures up to 900 C. *American Mineralogist: Journal of Earth and Planetary Materials* **1973**, *58* (7-8), 588-593.

(166) Brown, G.; Prewitt, C. High-temperature cystal chemistry of hortonolite. *American Mineralogist: Journal of Earth and Planetary Materials* **1973**, *58* (7-8), 577-587.

(167) Sciuto, P. F. On the presence of OH-groups in Zabagad olivine gems. *Neues Jahrbuch für Mineralogie Monatshefte* **1994**, *1994* (4), 145-156.

(168) Artioli, G.; Bellotto, M.; Palosz, B. High-temperature in situ Rietveld study of Fe, Mg cation partitioning in olivine. *Powder Diffraction* **1994**, *9* (1), 63-67.

(169) Della Giusta, A.; Ottonello, G.; Secco, L. Precision estimates of interatomic distances using site occupancies, ionization potentials and polarizability in Pbnm silicate olivines. *Acta Crystallographica Section B: Structural Science* **1990**, *46* (2), 160-165.

(170) Bragg, W.; Brown, G. XXX. Die Struktur des Olivins. *Zeitschrift für Kristallographie-Crystalline Materials* **1926**, *63* (1-6), 538-556.

(171) Heinemann, R.; Kroll, H.; Kirfel, A.; Barbier, B. Order and anti-order in olivine I: Structural response to temperature. *European journal of mineralogy* **2006**, *18* (6), 673-689.

(172) Lager, G. A.; Ross, F. K.; Rotella, F.; Jorgensen, J. Neutron powder diffraction of forsterite, Mg2SiO4: a comparison with single-crystal investigations. *Journal of Applied Crystallography* **1981**, *14* (2), 137-139.

(173) Kudoh, Y.; Kuribayashi, T.; Kagi, H.; Inoue, T. Cation vacancy and possible hydrogen positions in hydrous forsterite, Mg1. 985Si0. 993H0. 06O4, synthesized at 13.5 GPa and 1300 C. *Journal of Mineralogical and Petrological Sciences* **2006**, *101* (5), 265-269.

(174) Litvin A.L., S. V. P., Egorova L.N., Ostapenko S.S. Mg-Fe distribution in the structure of five olivines from meteorites. **1993**, *15*, 46, 54.

(175) Hushur, A.; Manghnani, M. H.; Smyth, J. R.; Nestola, F.; Frost, D. J. Crystal chemistry of hydrous forsterite and its vibrational properties up to 41 GPa. *American Mineralogist* **2009**, *94* (5-6), 751-760.

(176) Kudoh, Y.; Kuribayashi, T.; Litasov, K.; Ohtani, E. Cation vacancies and possible hydrogen atom positions in Fe-bearing hydrous forsterite, Mg1. 85Fe0. 14Si0. 99H0. 06O4, synthesized at 13.5 GPa and 1400° C. *Journal of Mineralogical and Petrological Sciences* **2007**, *102* (5), 306-310.

(177) Motoyama, T.; Matsumoto, T. The crystal structures and the cation distributions of Mg and Fe of natural olivines. *Mineralogical Journal* **1989**, *14* (8), 338-350.

(178) Aikawa, N.; Tokonami, M. Crystal structure and cation distribution of "cleavable" olivines. *Mineralogical Journal* **1987**, *13* (5), 271-279.

(179) Cernik, R.; Murray, P.; Pattison, P.; Fitch, A. A two-circle powder diffractometer for synchrotron radiation with a closed loop encoder feedback system. *Journal of Applied Crystallography* **1990**, *23* (4), 292-296.

(180) Ottonello, G.; Princivalle, F.; Della Giusta, A. Temperature, composition, and f O2 effects on intersite distribution of Mg and Fe 2+ in olivines: Experimental evidence and theoretical interpretation. *Physics and Chemistry of Minerals* **1990**, *17*, 301-312.

(181) Nestola, F.; Nimis, P.; Ziberna, L.; Longo, M.; Marzoli, A.; Harris, J. W.; Manghnani, M. H.; Fedortchouk, Y. First crystal-structure determination of olivine in diamond: Composition and implications for provenance in the Earth's mantle. *Earth and Planetary Science Letters* **2011**, *305* (1-2), 249-255.

(182) Liang, J.-J.; Hawthorne, F. C. Characterization of fine-grained mixtures of rock-forming minerals by Rietveld structure refinement; olivine+ pyroxene. *The Canadian Mineralogist* **1994**, *32* (3), 541-552.

(183) Basso, R.; Dal Negro, A.; Della Giusta, A.; Rossi, G. Fe/Mg distribution in the olivine of ultrafemic nodules from Assab (Ethiopia). **1979**.

(184) Angel, R. J.; Nestola, F. A century of mineral structures: How well do we know them? *American Mineralogist* **2016**, *101* (5), 1036-1045.

(185) Kudoh, Y.; Takeda, H. Single crystal X-ray diffraction study on the bond compressibility of fayalite, Fe2SiO4 and rutile, TiO2 under high pressure. *Physica B+ C* **1986**, *139*, 333-336.

(186) Yu, S.-C. Effects of pressure on the crystal structure of olivine in harzburgite xenolith of basalt. *Proceedings-National Science Council Republic of China part A Physical Science and Engineering* **1997**, *21*, 173-179.

(187) Princivalle, F.; Secco, L. Crystal structure refinement of 13 olivines in the Forsterite-Fayalite series from volcanic rocks and ultramafic nodules. *Tschermaks Mineralogische und Petrographische Mitteilungen* **1985**.

(188) Van der Wal, R.; Vos, A.; Kirfel, A. Conflicting results for the deformation properties of Forsterite, Mg2SiO4. *Acta Crystallographica Section B: Structural Science* **1987**, *43* (2), 132-143.

(189) Fujino, K.; Sasaki, S.; Takeuchi, Y.; Sadanaga, R. X-ray determination of electron distributions in forsterite, fayalite and tephroite. *Acta Crystallographica Section B: Structural Crystallography and Crystal Chemistry* **1981**, *37* (3), 513-518.

(190) Hazen, R. M. Effects of temperature and pressure on the crystal structure of forsterite. *American Mineralogist* **1976**, *61* (11-12), 1280-1293.

(191) Kudo Y., T. H. Fayalite, Fe2SiO4. *The Journal of the Japanese Association of Mineralogists, Petrologists and Economic Geologists* **1985**, *15*, 80.

(192) Müller-Sommer, M.; Hock, R.; Kirfel, A. Rietveld refinement study of the cation distribution in (Co, Mg)-olivine solid solution. *Physics and Chemistry of Minerals* **1997**, *24*, 17-23.

(193) Parker, S.; Catlow, C.; Cormack, A. Structure prediction of silicate minerals using energy-minimization techniques. *Acta Crystallographica Section B: Structural Science* **1984**, *40* (3), 200-208.

(194) Hazen, R. M. Effects of temperature and pressure on the crystal structure of ferromagnesian olivine. *American Mineralogist* **1977**, *62* (3-4), 286-295.

(195) Kirfel, A.; Lippmann, T.; Blaha, P.; Schwarz, K.; Cox, D.; Rosso, K.; Gibbs, G. Electron density distribution and bond critical point properties for forsterite, Mg 2 SiO 4, determined with synchrotron single crystal X-ray diffraction data. *Physics and chemistry of minerals* **2005**, *32*, 301-313.

(196) Finger, L. Fe/Mg ordering in olivines. *Carnegie Inst. Washington Year book* **1970**, *69*, 302-305.

(197) Mokeyeva, V.; EL, B.; ES, M. X-Ray Study of Details of Atomic Structure and Distribution of Magnesium and Iron Atoms In Lunar and Terrestrial Olivines. *Geochemistry International* **1976**.

(198) Heinemann, R.; Kroll, H.; Kirfel, A.; Barbier, B. Order and anti-order in olivine III: Variation of the cation distribution in the Fe, Mg olivine solid solution series with temperature and composition. *European Journal of Mineralogy* **2007**, *19* (1), 15-27.

(199) Ejima, T.; Akasaka, M.; Nagao, T.; Ohfuji, H. Occurrence of Fe3+ and formation process of precipitates within oxidized olivine phenocrysts in basalt lava from Kuroshima volcano, Goto islands, Nagasaki, Japan. *Mineralogical Magazine* **2015**, *79* (7), 1833-1848.

(200) Birle, J.; Gibbs, G.; Moore, P.; Smith, J. Crystal structures of natural olivines. *American Mineralogist: Journal of Earth and Planetary Materials* **1968**, *53* (5-6), 807-824.

(201) Heuer, M. The determination of site occupancies using a new strategy in Rietveld refinements. *Journal of Applied Crystallography* **2001**, *34* (3), 271-279.

(202) Akamatsu, T.; Kumazawa, M.; Aikawa, N.; Takei, H. Pressure effect on the divalent cation distribution in nonideal solid solution of forsterite and fayalite. *Physics and Chemistry of Minerals* **1993**, *19*, 431-444.

(203) Annersten, H.; Ericsson, T.; Filippidis, A. Cation ordering in Ni–Fe olivines. *American Mineralogist* **1982**, *67* (11-12), 1212-1217.

(204) Fisher, G. W.; Medaris Jr, L. G. Cell dimensions and X-ray determinative curve for synthetic Mg-Fe olivines. *American Mineralogist: Journal of Earth and Planetary Materials* **1969**, *54* (5-6), 741-753.

(205) Louisnathan, S.; Smith, J. Cell dimensions of olivine. *Mineralogical magazine and journal of the Mineralogical Society* **1968**, *36* (284), 1123-1134.

(206) Matsui, Y.; Syono, Y. Unit cell dimensions of some synthetic olivine group solid solutions. *Geochemical Journal* **1968**, *2* (1), 51-59.

(207) Merli, M.; Oberti, R.; Caucia, F.; Ungaretti, L. Determination of site population in olivine: Warnings on X-ray data treatment and refinement. *American Mineralogist* **2001**, *86* (1-2), 55-65.

(208) Urusov, V.; Lapina, I.; Kabalov, Y. K.; Kravchuk, I. Isomorphism in the forsterite-tephroite series. *Geokhimiya* **1984**, (7), 1047-1055.

(209) Yamazaki, S.; Toraya, H. Rietveld refinement of site-occupancy parameters of Mg2− xMnxSiO4 using a new weight function in least-squares fitting. *Journal of Applied Crystallography* **1999**, *32* (1), 51-59.

(210) Boström, D. Cation ordering at 1300 C in the (Ni, Mg)-olivine solid-solution series. *Acta Chemica Scandinavica* **1989**, *43*, 116-120.

(211) Zhang, D.; Hu, Y.; Xu, J.; Downs, R. T.; Hammer, J. E.; Dera, P. K. High-pressure behavior of liebenbergite: The most incompressible olivine-structured silicate. *American Mineralogist* **2019**, *104* (4), 580-587.

(212) Tamada, O.; Fujino, K.; Sasaki, S. Structures and electron distributions of α-Co2SiO4 and α-Ni2SiO4 (olivine structure). *Acta Crystallographica Section B: Structural Science* **1983**, *39* (6), 692-697.

(213) Lager, G.; Meagher, E. High-temperature structural study of six olivines. *American Mineralogist* **1978**, *63* (3-4), 365-377.

(214) De Waal, S. A.; Calk, L. C. Nickel minerals from Barberton, South Africa: VI. Liebenbergite, a nickel olivine. *American Mineralogist: Journal of Earth and Planetary Materials* **1973**, *58* (7-8), 733-735.

(215) Chen, J.; Li, R.; Parise, J. B.; Weidner, D. J. Pressure-induced ordering in (Ni, Mg) 2SiO4 olivine. *American Mineralogist* **1996**, *81* (11-12), 1519-1522.

(216) Hirschmann, M. M. *Studies of nickel and minor elements in olivine and in silicate liquids*; University of Washington, 1992.

(217) Pistorius, C. W. F. T. *Neues Jahrb. Mineral. Monatsh.* **1963**.

(218) Feier. British Museum (Natural History): London, United Kingdon.

(219) Lumpkin, G. R.; Ribbe, P. H. Composition, order-disorder and lattice parameters of olivines; relationships in silicate, germanate, beryllate, phosphate and borate olivines. *American Mineralogist* **1983**, *68* (1-2), 164-176.

(220) Miller, M. L.; Ribbe, P. H. Methods for determination of composition and intracrystalline cation distribution in Fe–Mn and Fe–Ni silicate olivines. *American Mineralogist* **1985**, *70* (7-8), 723-728.

(221) SHINNO, I. Relations between (130) spacing, chemical composition, and cation site preference of olivine. *The Journal of the Japanese Association of Mineralogists, Petrologists and Economic Geologists* **1980**, *75* (10), 343-352.

(222) Nishizawa, O.; Matsui, Y. An experimental study on partition of magnesium and manganese between olivine and orthopyroxene. *Physics of the Earth and Planetary Interiors* **1972**, *6* (5), 377-384.

(223) Akimoto, S. I.; Akaogi, M.; Kawada, K.; Nishizawa, O. Mineralogic distribution of iron in the upper half of the transition zone in the earth's mantle. *The geophysics of the Pacific Ocean Basin and its margin* **1976**, *19*, 399-405.

(224) Francis, C. A. Magnesium-manganese solid solution in the olivine and humite groups. **1980**.

(225) Sassi, M.; Kerisit, S. N. Ni and Co Incorporation in Forsterite: A Density Functional Theory Study with Hubbard Correction. *ACS Earth and Space Chemistry* **2024**, *8* (5), 1027-1038. DOI: 10.1021/acsearthspacechem.3c00370.

(226) Lumpkin, G. R.; Ribbe, P. H.; Lumpkin, N. E. Composition, order-disorder and lattice parameters of olivines; determinative methods for Mg-Mn and Mg-Ca silicate olivines. *American Mineralogist* **1983**, *68* (11-12), 1174-1182.

(227) Grandstaff, D. E. Changes in surface area and morphology and the mechanism of forsterite dissolution. *Geochimica et Cosmochimica Acta* **1978**, *42* (12), 1899-1901. DOI: https://doi.org/10.1016/0016-7037(78)90245-4.

(228) Awad, A.; van Groos, A. F. K.; Guggenheim, S. Forsteritic olivine: Effect of crystallographic direction on dissolution kinetics. *Geochimica et Cosmochimica Acta* **2000**, *64* (10), 1765-1772. DOI: 10.1016/s0016-7037(99)00442-1.

(229) King, H. E.; Satoh, H.; Tsukamoto, K.; Putnis, A. Surface-specific measurements of olivine dissolution by phase-shift interferometry. *American Mineralogist* **2014**, *99* (2-3), 377-386.

(230) Chung-Cherng, L.; Pouyan, S. Directional dissolution kinetics of willemite. *Geochimica et cosmochimica acta* **1993**, *57* (1), 27-35.

(231) Li, X.; Shen, X.; Wang, Q.; Lu, D.; Qian, B.; Pedrosa, E. T.; Luttge, A. Influence of surface orientation on the variability of olivine dissolution rates. *Applied Surface Science* **2024**, 159634.

(232) Demouchy, S. Defects in olivine. *Eur. J. Mineral.* **2021**, *33* (3), 249-282. DOI: 10.5194/ejm-33-249-2021.